Principal component analysis of anisotropic finite-frequency sensitivity kernels

Anne Sieminski, Jeannot Trampert, Jeroen Tromp

Geophys. J. Int. (2009) **179,** 1186–1198 doi: 10.1111/j.1365-246X.2009.04341.x

Principal component analysis of anisotropic finite-frequency sensitivity kernels

Anne Sieminski,[1] Jeannot Trampert[2] and Jeroen Tromp[3]

[1] *Laboratoire de Géophysique Interne et Tectonophysique, CNRS, Université Joseph Fourier, Grenoble, France. E-mail: anne.sieminski@obs.ujf-grenoble.fr*
[2] *Department of Earth Sciences, Utrecht University, Utrecht, The Netherlands*
[3] *Department of Geosciences and Program in Applied and Computational Mathematics, Princeton University, Princeton, NJ, USA*

Accepted 2009 July 20. Received 2009 June 20; in original form 2009 May 15

SUMMARY

We use a principal component analysis to characterize the finite-frequency sensitivity of seismic observables to anisotropy. A general anisotropic medium may be described in terms of 21 independent elastic parameters, each of which has an associated 'primary' sensitivity kernel. Our principal component analysis ranks linear combinations of the primary kernels to ascertain the dominant anisotropic parameters associated with a particular seismic observable. The principal parameters are those to which a given data set is the most sensitive. We demonstrate the efficiency of the method for a single arrival associated with a particular source–receiver combination, and apply it to a small synthetic Love-wave data set with a simple source–receiver geometry. For direct body wave arrivals, such as *P, S* and *SKS*, and direct Love and Rayleigh surface waves, our principal component analysis finds the same small combinations of dominant anisotropic parameters previously identified based upon asymptotic methods. The analysis further confirms the importance of mode coupling in finite-frequency surface wave sensitivity kernels. Our approach can be directly incorporated into a tomographic inversion to automatically select the general anisotropic parameters which are best constraint, for example, without prescribing the model to be transversely isotropic with a particular symmetry axis. The computational overhead associated with the calculation of the 21 primary kernels and the subsequent principal component analysis is minimal relative to an isotropic calculation.

Key words: Inverse theory; Seismic anisotropy; Seismic tomography; Computational seismology.

1 INTRODUCTION

The desire to extend the limits of asymptotic (ray-based) tomography has resulted in an intense study of finite-frequency seismic wave propagation. These studies have revealed complicated 3-D sensitivity patterns of seismic data to structural parameters (e.g. Marquering *et al.* 1999; Zhou *et al.* 2004; Zhao *et al.* 2005; Liu & Tromp 2006; Zhao & Jordan 2006; Liu & Tromp 2008; Zhou 2009). In the presence of anisotropy, the large number of elastic parameters (21 in the most general case) makes it difficult to objectively assess their relative importance (Sieminski *et al.* 2007a,b; Panning & Nolet 2008). Such an assessment is critical for successful, unbiased mantle imaging.

Seismic anisotropy is an essential aspect of the elastic structure of the Earth's mantle, well documented by seismic observations of shear wave splitting (Vinnik *et al.* 1989), the Love–Rayleigh discrepancy (Anderson 1961), and azimuthal variations of surface wave (Forsyth 1975) and refracted *P*-wave speeds (Hess 1964; Backus 1965). Anisotropy is thought to be the result of preferential orientation of anisotropic minerals due to large-scale deformation and flow (e.g. Zhang & Karato 1995; Kaminski & Ribe 2002). Mapping seismic anisotropy can therefore provide information on past- and present-mantle dynamics (e.g. Silver 1996; Montagner 1998; Debayle *et al.* 2005; Deschamps *et al.* 2008). General anisotropy is described by 21 elastic parameters, but it is currently impossible to image all of these parameters throughout the mantle. New data and observables would need to be collected and identified to determine such a large number of parameters with satisfactory resolution. More fundamentally, we anticipate that seismic data cannot resolve all the anisotropic aspects of a medium, simply because seismic waves do not sample the Earth's structure in all directions (Maupin & Park 2007).

The key to imaging mantle anisotropy is therefore to find the few relevant elastic parameters which explain most of the data. A possible strategy is to fix the mineralogy *a priori*, for instance by assuming hexagonal symmetry (or transverse isotropy) with horizontal, vertical or tilted symmetry axes (Chevrot 2006; Long *et al.* 2008; Panning & Nolet 2008). This is supported by Becker *et al.*'s (2006) study showing that anisotropy in the Earth's upper mantle is dominated by hexagonal symmetry with strong correlations

between the elastic parameters. Another approach is to estimate those parameters to which the data are most sensitive. This was proposed by Montagner & Jobert (1988) for mantle tomography utilizing fundamental-mode surface waves. Based upon the depth sensitivity of asymptotic surface waves calculated in a 1-D reference mantle model, Montagner & Nataf (1986) retained only three dominant parameters. Subsequent surface wave tomography of azimuthal anisotropy extended this approach (Montagner & Tanimoto 1991; Lévêque *et al.* 1998; Simons *et al.* 2002; Debayle *et al.* 2005).

We present a quantitative analysis of finite-frequency sensitivity of seismic observables to general anisotropy. The idea is to extract the 'principal parameters', that is, those elastic parameters to which the data are most sensitive. The principal parameters are linear combinations of the 21 'primary' components of the elastic tensor. The approach involves a principal component analysis of the sensitivity kernels, as explained in Section 2. To demonstrate the efficiency of the method, we apply it in Section 3 to single source–receiver sensitivity kernels for traveltime data commonly used in mantle imaging. More generally, in a tomographic inverse problem, the sensitivity to an entire data set should be considered. In this context, we test our approach for a simple synthetic tomographic experiment in Section 4, before discussing its potential for realistic imaging in Section 5.

2 PRINCIPAL COMPONENT ANALYSIS

The elastic properties of a medium are generally described by the fourth-order elastic tensor c_{klmn}, $(k, l, m, n = 1, 2, 3)$ linking stress and strain according to Hooke's law. Because of various symmetries, the elastic tensor has only 21 independent components, which are often written using Voigt's notation as C_{IJ}, $(I, J = 1, \ldots, 6)$ (Babuška & Cara 1991). Appendix A summarizes the relationships between these two complementary descriptions. In the following, we use the notation c_i, $(i = 1, \ldots, 21)$ to describe the 21 independent components of the elastic tensor. Studies of seismic wave propagation in weakly anisotropic media prefer to use linear combinations of the c_i, such as Thomsen's parameters (Thomsen 1986; Chevrot 2006; Panning & Nolet 2008) or the 'asymptotic parameters' (Chen & Tromp 2007) written here as a_i, $(i = 1, \ldots, 21)$. The definition of the asymptotic parameters is given in Appendix A; these parameters appear naturally when considering asymptotic seismic wave propagation in weakly anisotropic media (Smith & Dahlen 1973; Montagner & Nataf 1986; Chen & Tromp 2007) and are commonly used in surface wave tomography (e.g. Montagner & Tanimoto 1991; Trampert & van Heijst 2002; Debayle *et al.* 2005; Marone & Romanowicz 2007). The asymptotic parameters emphasize the directional dependence of wave propagation in anisotropic media (Table 1).

The sensitivity of seismic data to structural parameters is given by Fréchet derivatives K_m, $m = 1, \ldots, 21$, (hereafter referred to as 'sensitivity kernels'), which describe how perturbations in structural parameters, δm, affect observables, δo

$$\delta o = \int K_m(\mathbf{x}) \delta m(\mathbf{x}) \, \mathrm{d}^3\mathbf{x}, \tag{1}$$

where the integral is taken over the Earth's volume. We seek linear combinations of the basic anisotropic kernels $K_{c_i}, i = 1, \ldots, 21$, which maximize the 'sensitivity power'. We define the sensitivity power as $\int [K_m(\mathbf{x})]^2 \, \mathrm{d}^3\mathbf{x}$ and write $K_p = \sum_j w_j K_{c_j}$, where p labels a specific linear combination and w_j, $j = 1, \ldots, 21$, are the corresponding coefficients. With these definitions, our maximization problem is

$$\frac{\int \left[K_p(\mathbf{x})\right]^2 \, \mathrm{d}^3\mathbf{x}}{\int \mathrm{d}^3\mathbf{x}} = \frac{\int \left[\sum_j w_j K_{c_j}(\mathbf{x})\right]^2 \, \mathrm{d}^3\mathbf{x}}{\int \mathrm{d}^3\mathbf{x}} = \text{maximum} \equiv \lambda, \tag{2}$$

subject to the condition $\sum_j w_j^2 = 1$. The maximization problem (2) is equivalent to the eigenvalue problem

$$\mathbf{M}\mathbf{w} = \lambda \mathbf{w}, \tag{3}$$

where the components of the symmetric, positive-definite 21×21-dimensional matrix $\mathbf{M}$ are

$$M_{ij} = \frac{\int K_{c_i}(\mathbf{x}) K_{c_j}(\mathbf{x}) \, \mathrm{d}^3\mathbf{x}}{\int \mathrm{d}^3\mathbf{x}}. \tag{4}$$

The 21-dimensional vectors $\mathbf{w}_k$ satisfying eq. (3) are the orthonormal eigenvectors of $\mathbf{M}$ with associated eigenvalues λ_k. The 21 principal kernels K_{p_k} associated with the eigenvalues λ_k are thus

$$K_{p_k} = \sum_j w_{kj} K_{c_j}, \tag{5}$$

where w_{kj} denotes the jth component of the kth eigenvector. Ordering the λ_k by decreasing value, the principal kernels are such that

$$\int \left[K_{p_1}(\mathbf{x})\right]^2 \, \mathrm{d}^3\mathbf{x} > \int \left[K_{p_2}(\mathbf{x})\right]^2 \, \mathrm{d}^3\mathbf{x} > \cdots > \int \left[K_{p_k}(\mathbf{x})\right]^2 \, \mathrm{d}^3\mathbf{x} > \cdots > \int \left[K_{p_{21}}(\mathbf{x})\right]^2 \, \mathrm{d}^3\mathbf{x}. \tag{6}$$

The principal kernels satisfy the orthogonality relation

$$\frac{\int K_{p_k}(\mathbf{x}) K_{p_l}(\mathbf{x}) \, \mathrm{d}^3\mathbf{x}}{\int \mathrm{d}^3\mathbf{x}} = \lambda_k \, \delta_{kl}. \tag{7}$$

They are therefore linearly independent and describe the principal (essential) spatial patterns of sensitivity to anisotropy. The elastic parameters p_k corresponding to the principal kernels K_{p_k} are obtained from the basic parameters c_j based upon the relation

$$p_k = \sum_j w_{kj} c_j. \tag{8}$$

If the data have limited resolving power, we expect that for some positive integer $n \leq 21$ the eigenvalues λ_k for $k > n$ become negligible. If the number n is small (e.g. less than 3 or 4), it is possible

Table 1. Azimuthal dependence associated with the 21 elastic parameters describing asymptotic seismic wave propagation in weakly anisotropic media (Montagner & Nataf 1986; Chen & Tromp 2007).

Elastic parameters	Azimuthal dependence
$A\ C\ N\ L\ F$	0ξ
$J_c\ J_s\ K_c\ K_s\ M_c\ M_s$	1ξ
$B_c\ B_s\ H_c\ H_s\ G_c\ G_s$	2ξ
$D_c\ D_s$	3ξ
$E_c\ E_s$	4ξ

Notes: The angle ξ is the azimuth along the geometrical ray path. The parameters A, C, N, L and F describe anisotropy with hexagonal symmetry and a vertical (or radial) symmetry axis. These five parameters do not cause an azimuthal dependence. The parameters producing azimuthal anisotropy are organized in pairs, the 'c' parameters correspond to a dependence on $\cos n\xi$ and the 's' parameters to a dependence on $\sin n\xi$ (with $n = 1, 2, 3, 4$).

to invert for the parameters associated with the first n principal parameters p_k, $k = 1, \ldots, n$. This results in an inverse problem of manageable size and guarantees that the model parameter bias will be small, because we only neglected parameters with small sensitivity power.

We compute the basic sensitivity kernels K_{c_i}, $i = 1, \ldots, 21$, using a combination of Spectral-Element Simulations of seismic wave propagation and Adjoint MEthods (SESAME). This method is fully described in Tromp *et al.* (2005) and Liu & Tromp (2006, 2008) for the general case, and in Sieminski *et al.* (2007a,b) for specific applications to anisotropic sensitivity kernels. In the adjoint approach (e.g. Tarantola 1984), sensitivity kernels are constructed based upon the interaction of the 'regular' wavefield, propagating from the source to the receiver(s), with an 'adjoint' wavefield, propagating from the receiver(s) to the source. The nature of the interaction depends on the specific structural parameters. The adjoint wavefield is generated at the receiver location(s) by an adjoint point-force source, which depends on the data. In SESAME, the regular and adjoint wavefields are simulated using a spectral-element method (Komatitsch & Tromp 2002a,b). The principal component analysis of anisotropy presented here can be applied to sensitivity kernels calculated using any other numerical or analytical approach.

Strictly speaking, the volume integrals in eq. (4) should be evaluated over the Earth's volume. The sensitivity kernels are in general only significant in a limited zone around the source–receiver path and the volume integrals can therefore be restricted to a smaller domain. We only consider one chunk of the 'cubed-Earth' (Komatitsch & Tromp 2002a,b) with a $30^\circ \times 30^\circ$ surface area in which the sensitivity kernels are numerically computed. Sensitivity kernels constructed based upon SESAME reflect the source radiation pattern near the hypocentre (Liu & Tromp 2008). This gives the sensitivity a very specific pattern in the vicinity of the source location. Because the volume of this source region is very small, it does not significantly contribute to the principal characteristics of the sensitivity. We therefore exclude the near-field zone around the source in our tests, which is defined by one and two wavelengths around the hypocentre for surface waves and body waves, respectively. Finally, the adjoint spectral-element kernels must be slightly smoothed before being analysed to remove any spurious values, especially in the vicinity of the sources and receivers. As in Tape *et al.* (2007), we convolve the kernels with a 3-D Gaussian. In Section 3, the half-width of the Gaussian function is selected based upon the minimum wavelength the mesh can resolve. This choice will, however, be revisited for the experiment in Section 4.

3 APPLICATION TO SINGLE MEASUREMENTS

3.1 Fundamental-mode surface waves

We first apply the principal component analysis to single source–receiver sensitivity kernels of surface waves. The 21 basic kernels K_{c_i} are numerically computed using SESAME and are accurate for periods longer than 15 s. The background model is the spherically symmetric, isotropic Preliminary Reference Earth Model (PREM; Dziewonski & Anderson 1981). The source mechanism is the Harvard centroid-moment tensor solution for the 1994 June 9 Bolivia earthquake (www.globalcmt.org). We locate it at 15 km depth to generate a strong fundamental-mode signal. The half duration is also modified and set to 8 s to be compatible with the resolution of the spectral-element mesh. We analyse fundamental mode Love and Rayleigh waves with periods between 40 and 100 s at two hypothetical stations (labelled A and B). The stations are located at an epicentral distance of 50° and correspond to different source azimuthal angles (150° and 110° from due south). Due to the source radiation pattern, station A mainly receives Rayleigh-wave energy whereas station B mainly receives Love-wave energy (Fig. 1).

To isolate the fundamental mode between 40 and 100 s, the synthetic signals are time-variable filtered (Landisman *et al.* 1969).

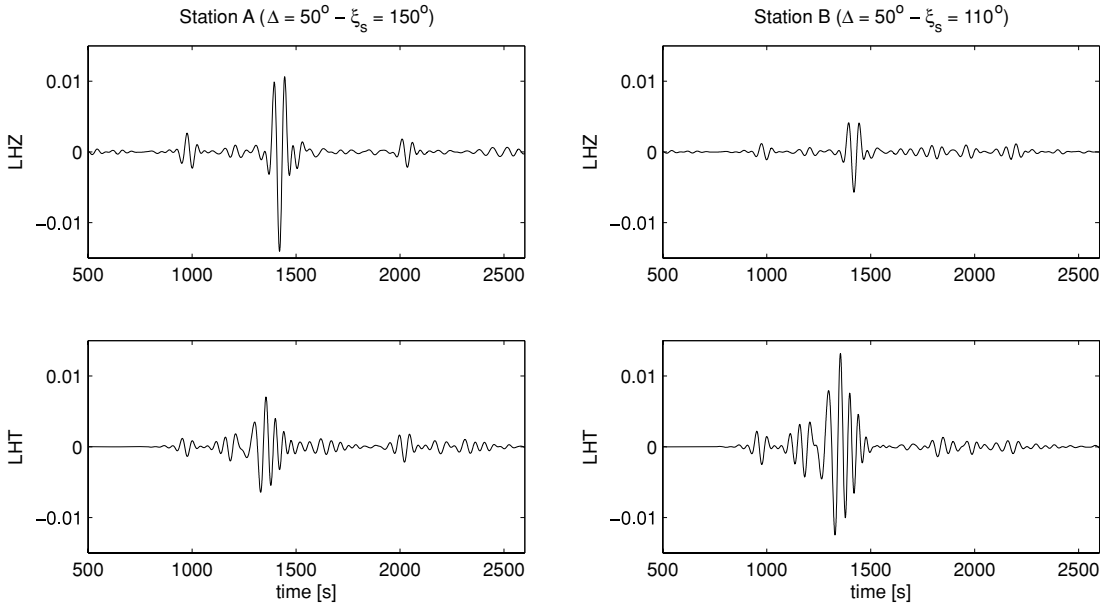

Figure 1. Vertical (top panel) and transverse (bottom panel) displacement seismograms calculated at station A (left-hand panels) and station B (right-hand panels) for the Bolivia source mechanism located at 15 km depth in isotropic PREM. The epicentral distance is denoted by Δ and the source azimuthal by ξ_s. The signals are filtered between 40 and 100 s. Because of the source radiation pattern, station A receives more Rayleigh-wave energy (vertical component LHZ) and station B more Love-wave energy (transverse component LHT).

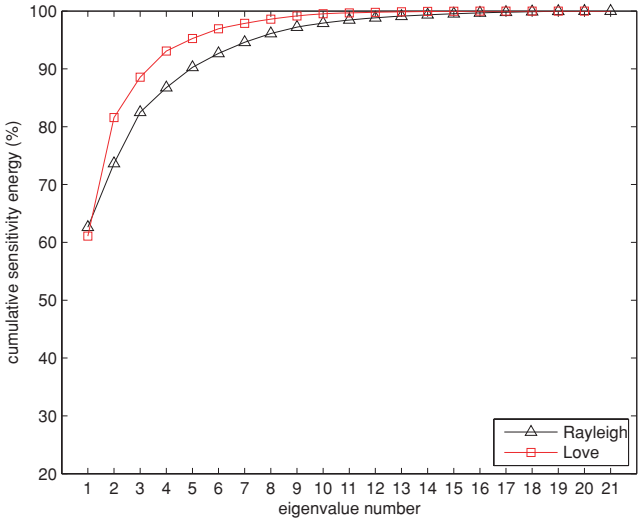

Figure 2. Cumulative sensitivity power $(\sum_{k=1}^{n} \int [K_{p_k}(\mathbf{x})]^2 \, \mathrm{d}^3\mathbf{x} / \sum_{k=1}^{21} \int [K_{p_k}(\mathbf{x})]^2 \, \mathrm{d}^3\mathbf{x})$ for the 21 principal parameters p_k determined from the principal component analysis (Section 2) of the single source–receiver sensitivity for the fundamental-mode Rayleigh wave recorded at station A (triangles) and the fundamental-mode Love wave recorded at station B (squares) (Fig. 1). The epicentral distance is 50° for both stations. We consider waves in the period range from 40 to 100 s.

The adjoint-source time functions are constructed from the time-variable filtered signals. We analyse the sensitivity of the traveltime of these waves as if measured by cross-correlation (Marquering *et al.* 1999; Tromp *et al.* 2005). The cross-correlation traveltime is equivalent to classical phase adjustments in surface wave processing (Sieminski *et al.* 2007a). We follow the convention of a positive traveltime anomaly for a delay of the observed waves relatively to the reference.

Fig. 2 shows the cumulative sensitivity power determined for Rayleigh and Love waves. In these examples the sensitivity is captured by a small number of parameters: about 90 per cent of the total sensitivity power is contained in three principal kernels for Love waves and five for Rayleigh waves. In particular, the first principal kernel K_{p_1} carries most of the sensitivity (about 60 per cent of the total power in both cases). The principal kernels K_{p_k} are initially found as linear combinations of the basic anisotropic kernels K_{c_j} (eq. 5). It is however more meaningful to express the principal kernels as linear combinations of the asymptotic parameters a_i, because the asymptotic parameters are more readily interpreted physically (Montagner & Nataf 1986; Chen & Tromp 2007). In the following, we write

$$K_{p_k} = \sum_i u_{ki} K_{a_i} . \tag{9}$$

The coefficients u_{ki} are shown in Figs 3 and 4 for the first three principal Love and Rayleigh kernels. For the Love wave, the largest coefficients u_{ki} are attributed to the parameters N and $E_{c,s}$ and then $M_{c,s}$ and $D_{c,s}$ (Fig. 3). For the Rayleigh wave, we find the dominant parameters L and $G_{c,s}$ and then $M_{c,s}$ and $D_{c,s}$ (Fig. 4). These parameters are simply those for which fundamental-mode Love- and Rayleigh-wave sensitivity is broadly distributed in depth (Sieminski *et al.* 2007a). As we seek to maximize the sensitivity power integrated over the crust and mantle, these parameters dominate. Rayleigh-wave sensitivity to the parameters $E_{c,s}$ is large and laterally extended (Sieminski *et al.* 2007a), but it is restricted to very shallow structure and therefore does not have a large sensitivity power when integrated over the crust and mantle. Based upon asymptotic wave propagation, the parameters N, $E_{c,s}$ and L, $G_{c,s}$ were already identified as the primary ones for Love and Rayleigh waves, respectively (Montagner & Jobert 1988). This is not surprising because the asymptotic description effectively predicts the sensitivity with depth of finite-frequency fundamental-mode surface waves (Sieminski *et al.* 2007a). The parameters $M_{c,s}$ and $D_{c,s}$ are involved in SV–SH coupling (Chen & Tromp 2007). They appear here because the sensitivity kernels are calculated considering full-wave propagation, which includes Love–Rayleigh coupling. The spatial pattern of the principal sensitivity kernels (Figs 3 and 4) directly reflects these effects. The first two principal Love-wave kernels K_{p_1} and K_{p_2} present an elliptical Fresnel-zone pattern, modified by an azimuthal dependence for K_{p_2} because we have $K_{p_2} \simeq -K_{E_s}$, E_s being a 4ξ azimuthal parameter (Table 1). The same is observed for the first two principal Rayleigh-wave kernels ($K_{p_2} \simeq -K_{G_s}$ and G_s being a 2ξ azimuthal parameter), but the third principal Rayleigh-wave kernel K_{p_3} clearly displays 'V' bands of alternating positive and negative amplitude. While the elliptical pattern is described by self-coupling in a Born-scattering formalism, the V-band pattern indicates Love–Rayleigh coupling (Sieminski *et al.* 2007a).

The first Rayleigh-wave principal kernel in Fig. 4 shows at first glance a counter-intuitive positive amplitude. However, the corresponding first principal parameter p_1 is a combination of the parameters L and G_s given by $p_1 \simeq -L - G_s$ (eq. 8 and Fig. 4). A negative perturbation of the parameter L (i.e. a decrease of the SV-wave speed) therefore gives a positive perturbation of the parameter p_1, which results in a positive traveltime anomaly, that is, a delay in our convention.

3.2 Body waves

In a second series of experiments, the principal component analysis is applied to single source–receiver sensitivity kernels for body wave traveltime data. The configuration is the same as for the surface waves, except that the Bolivia earthquake source mechanism is now located at its original depth of 647 km to obtain clear body wave arrivals. We investigate the sensitivity of P-wave cross-correlation traveltime measurements and the sensitivity of S- and SKS-wave splitting intensity.

For the P-wave cross-correlation traveltime, the vertical component of the adjoint source is constructed from the time-derivative of the vertical signal in the P-wave time window (Tromp *et al.* 2005; Sieminski *et al.* 2007b). To study the S-wave sensitivity we must use an observable that characterizes shear wave splitting caused by anisotropy. The splitting intensity is such an observable. It was originally defined for SKS waves as the amplitude of the transverse signal relative to the radial signal in the SKS time window (Chevrot 2000, 2006). For weak anisotropy, the SKS-splitting intensity can be efficiently retrieved by cross-correlating the radial signal with the sum of the radial and transverse signal (Sieminski *et al.* 2008). With the latter definition, the corresponding adjoint-source function is constructed from the time-derivative of the radial signal on the transverse component. The splitting intensity is extended to S waves by identifying the radial direction with the initial polarization direction of the waves before they are affected by anisotropy or with the polarization in an isotropic reference model (Long *et al.* 2008). The corresponding transverse direction is then the orthogonal direction in the horizontal plane. We analyse the sensitivity of P-wave traveltime and S-wave splitting intensity for periods longer than 15 s recorded at an epicentral distance of 50°. The sensitivity of

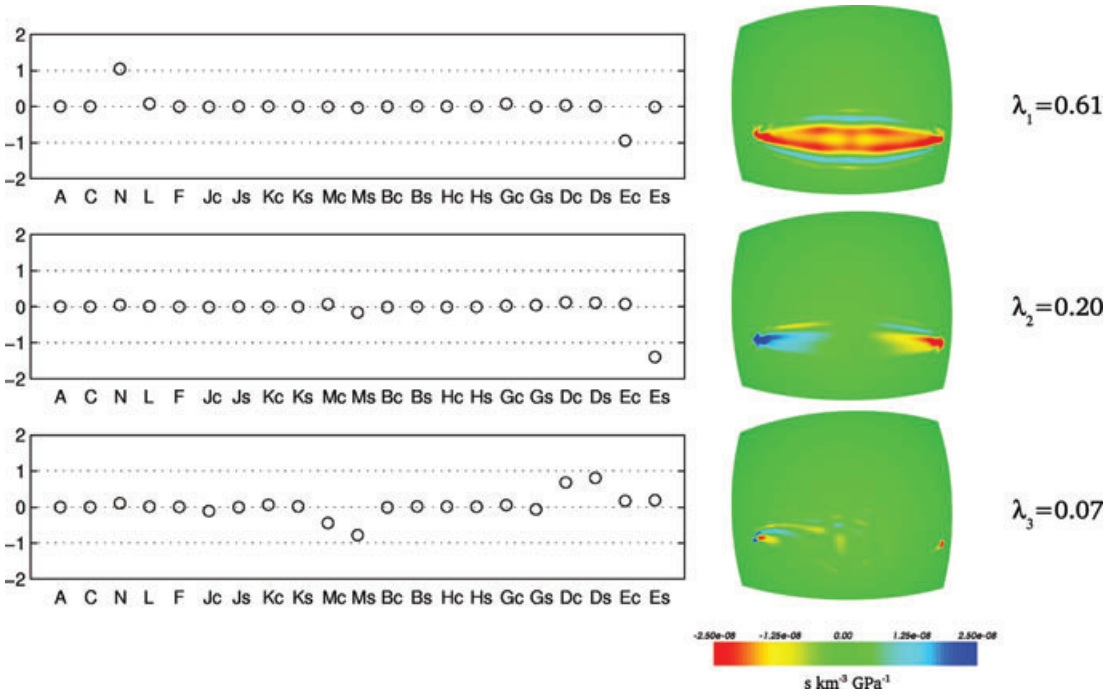

Figure 3. First three principal sensitivity kernels for the fundamental-mode Love wave: (left-hand panels) coefficients u_{ki} of the linear combination linking the principal kernels K_{p_k} to the 21 asymptotic kernels K_{a_i} and (right-hand panels) spatial patterns of the kernels in map view at 75 km depth (the source is on the left-hand side). The coefficients u_{ki} are linear combinations of the components of the kth eigenvector and are defined such that $K_{p_k} = \sum u_{ki} K_{a_i}$ (eq. 9). The quantities λ_k are the corresponding eigenvalues normalized such that $\sum_l \lambda_l = 1$.

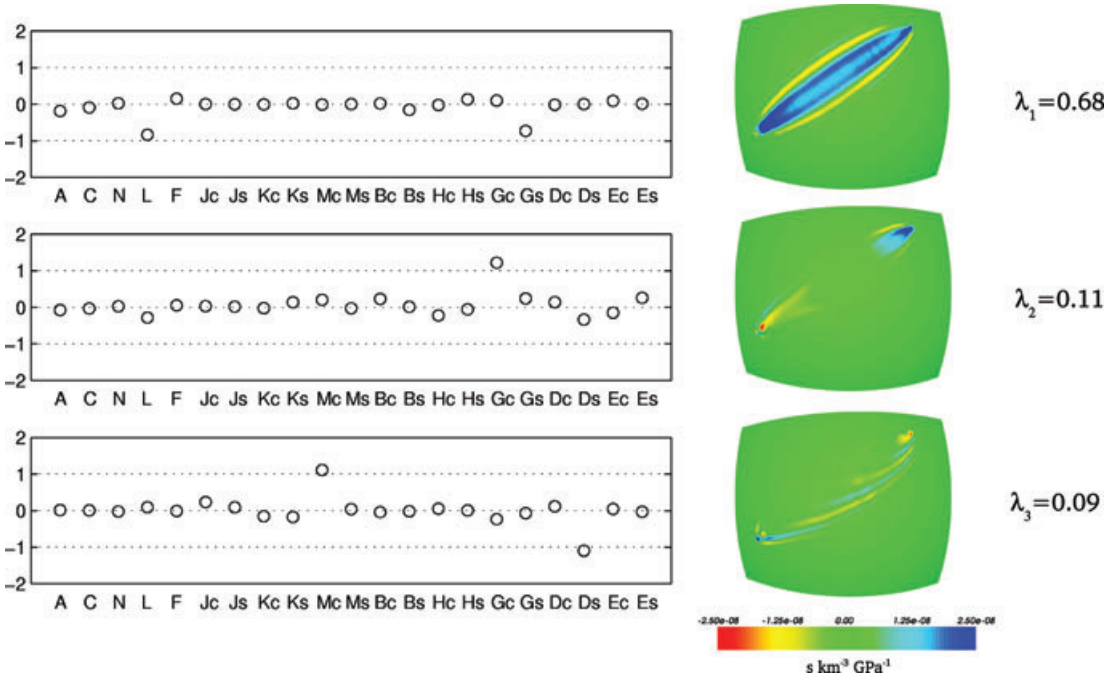

Figure 4. First three principal sensitivity kernels for the fundamental-mode Rayleigh wave: (left-hand panels) coefficients u_{ki} of the linear combination linking the principal kernels K_{p_k} to the 21 asymptotic kernels K_{a_i} (eq. 9) and (right-hand panels) spatial patterns of the kernels in map view at 75 km depth.

the *SKS*-wave splitting intensity is analysed for periods longer than 13 s recorded at an epicentral distance of 105°.

As for surface waves, nearly 90 per cent of the total power of the sensitivity is reached with a small number of principal kernels: two principal kernels for the *SKS* wave, three kernels for the *P* wave and four kernels for the *S* wave (Fig. 5). The values of the coefficients u_{ki} (eq. 9) clearly show that *SKS* splitting is mainly sensitive to the $G_{c,s}$ parameters (Fig. 6), as often assumed (Montagner *et al.* 2000; Favier & Chevrot 2003; Chevrot 2006). The parameters $G_{c,s}$ are indeed simply linked to Thomsen's parameter γ (Sieminski *et al.* 2007b, 2008) as used by Favier & Chevrot (2003) and Chevrot (2006). As expected, the principal sensitivity kernels are focused on

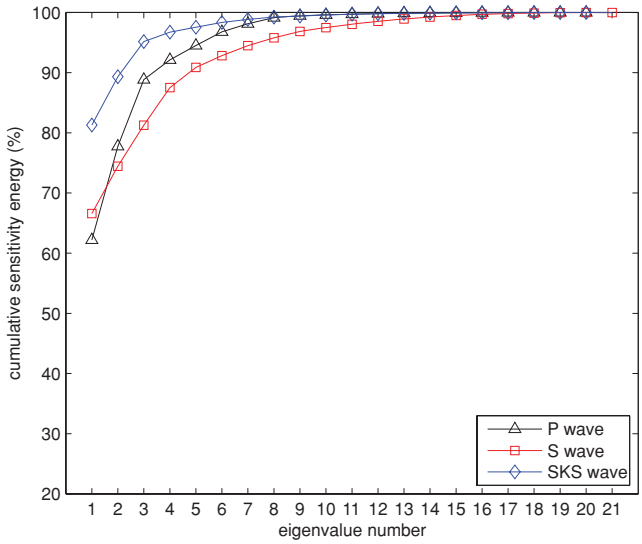

Figure 5. Cumulative sensitivity power for the 21 principal parameters p_k for the *P*-wave traveltime (triangles), the *S*-wave splitting intensity (squares) and the *SKS*-wave splitting intensity (diamonds). For *P* and *S* waves, the epicentral distance is 50° and we consider waves in the period range from 15 to 300 s. For the *SKS* wave, the epicentral distance is 105° and the period range is from 13 to 300 s.

a narrow and shallow region beneath the receiver (Favier & Chevrot 2003; Sieminski *et al.* 2008) (Fig. 6). For *P* waves, the dominant parameters are $J_{c,s}$ and $K_{c,s}$, which again have previously been identified as the important parameters for asymptotic *P*-wave propagation in weakly anisotropic media (Chen & Tromp 2007). We note the relatively small contribution of the transversely isotropic parameters (A, C and F) from which the isotropic *P*-wave speed is defined. The first principal sensitivity kernels are focused on a small region beneath the receiver in Fig. 7. However, the spatial pattern of the sensitivity strongly depends on the source location and more pronounced sensitivity would be observed on the source side for a shallower event. More parameters are needed to describe asymptotic *S*-wave propagation in weakly anisotropic media (Chen & Tromp 2007). This is confirmed by the principal component analysis of the *S*-wave splitting sensitivity. A large number of asymptotic kernels are involved in describing the principal kernels (Fig. 8). We identify the dominant parameters as $M_{c,s}$, $D_{c,s}$, $K_{c,s}$ and N for the case shown in Fig. 8. The spatial pattern of the principal kernels is very similar to the *P*-wave case, with foci of sensitivity beneath the receiver and in the vicinity of the source, and with little sensitivity in-between. This *S*-wave sensitivity is a good example of a situation where the principal component analysis identifies a small number of independent combinations of a large number of asymptotic parameters.

3.3 Fundamental-mode surface waves with strong mode-coupling

In Section 3.1, we investigated surface wave sensitivity under circumstances involving limited mode coupling. Still, coupling is present as shown by the significant contributions of the parameters $M_{c,s}$ and $D_{c,s}$ and the spatial pattern of the principal Rayleigh-wave kernel K_{p_3} (Fig. 4). To analyse the effects of mode coupling in greater detail, we now consider the Love wave at station A and the Rayleigh wave at station B; the experimental setting is the same as in Section 3.1. Because the source directs more Rayleigh-wave energy to station A (and more Love-wave energy to station B) (Fig. 1), the Love-wave signal at station A (the Rayleigh-wave signal at station B) is expected to be strongly affected by Rayleigh–Love coupling (Love–Rayleigh coupling). Six to seven principal kernels are needed to reach 90 per cent of the total sensitivity power (Fig. 9). The kernels related to the parameters N and $E_{c,s}$ for the Love wave (Fig. 10) and L and $G_{c,s}$ for the Rayleigh wave (Fig. 11) still contribute significantly to the principal kernels, but the major parameters are now the SV–SH coupling parameters $M_{c,s}$ and $D_{c,s}$. Accordingly, the first principal kernels for Love and Rayleigh waves show the characteristic alternating positive and negative V bands due to Love–Rayleigh coupling as interpreted from a Born-scattering formalism (Sieminski *et al.* 2007a). The number of significant principal components is still small compared to 21, although in practise it would seem challenging to constrain the structure with six or seven dominant parameters. This is an extreme case however.

It is important to keep in mind that the sensitivity characteristics are path dependent. We illustrate this by comparing the sensitivity kernels of the Love wave recorded at station B and at a third station

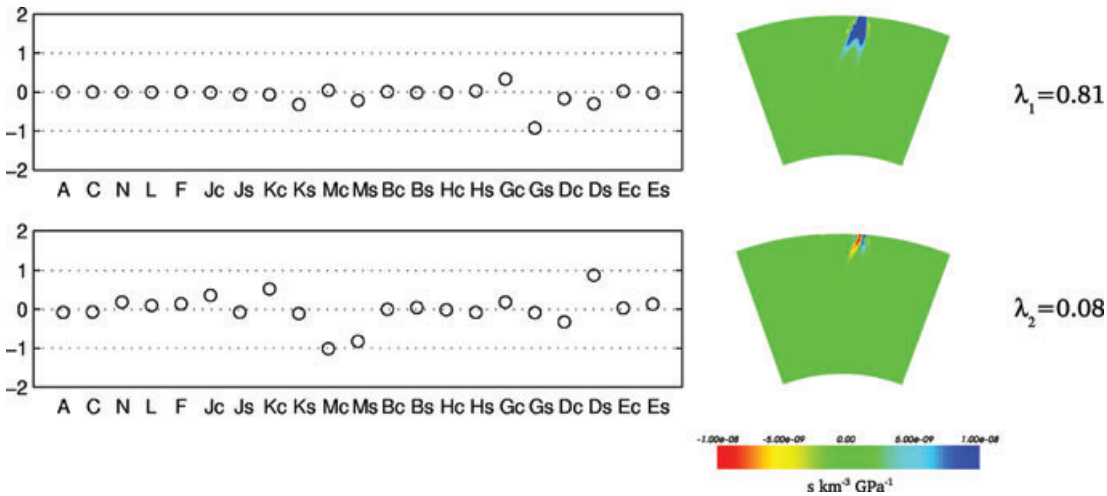

Figure 6. First two principal sensitivity kernels for the *SKS*-wave splitting intensity: (left-hand panels) coefficients u_{ki} of the linear combination linking the principal kernels K_{p_k} to the 21 asymptotic kernels K_{a_i} (eq. 9) and (right-hand panels) spatial patterns of the kernels plotted in the vertical source–receiver plane and zooming in on the receiver side (*SKS*-splitting is not sensitive to the structure until the wave exits the core).

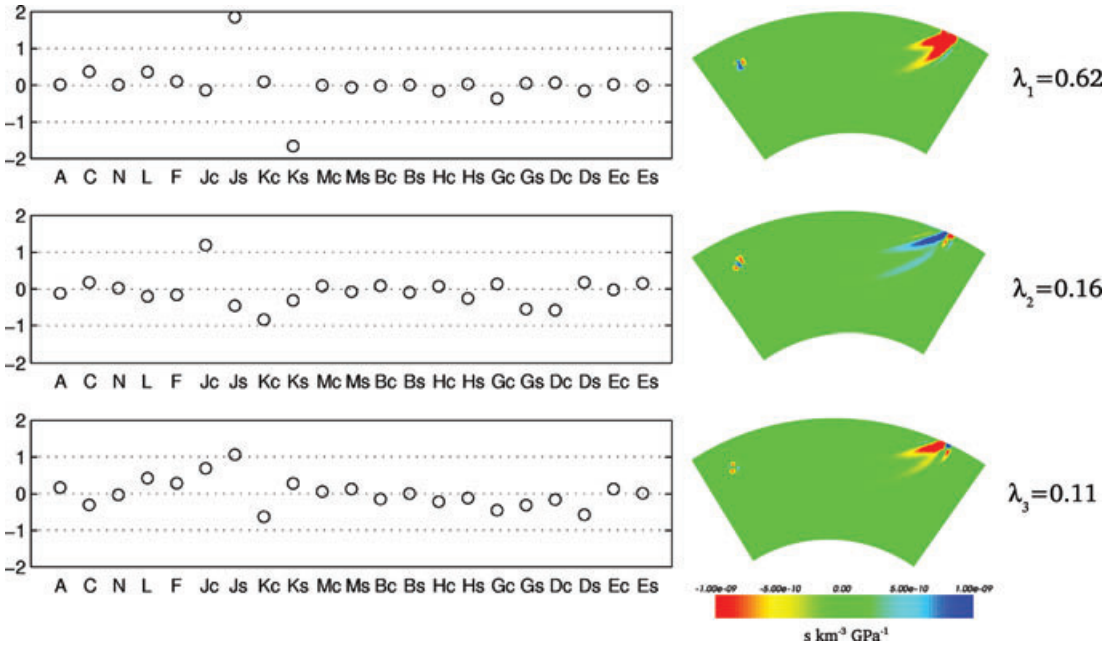

Figure 7. First three principal sensitivity kernels for the *P*-wave traveltime: (left-hand panels) coefficients u_{ki} of the linear combination linking the principal kernels K_{p_k} to the 21 asymptotic kernels K_{a_i} (eq. 9) and (right-hand panels) spatial patterns of the kernels plotted in the vertical source–receiver plane (the source is on the left-hand side).

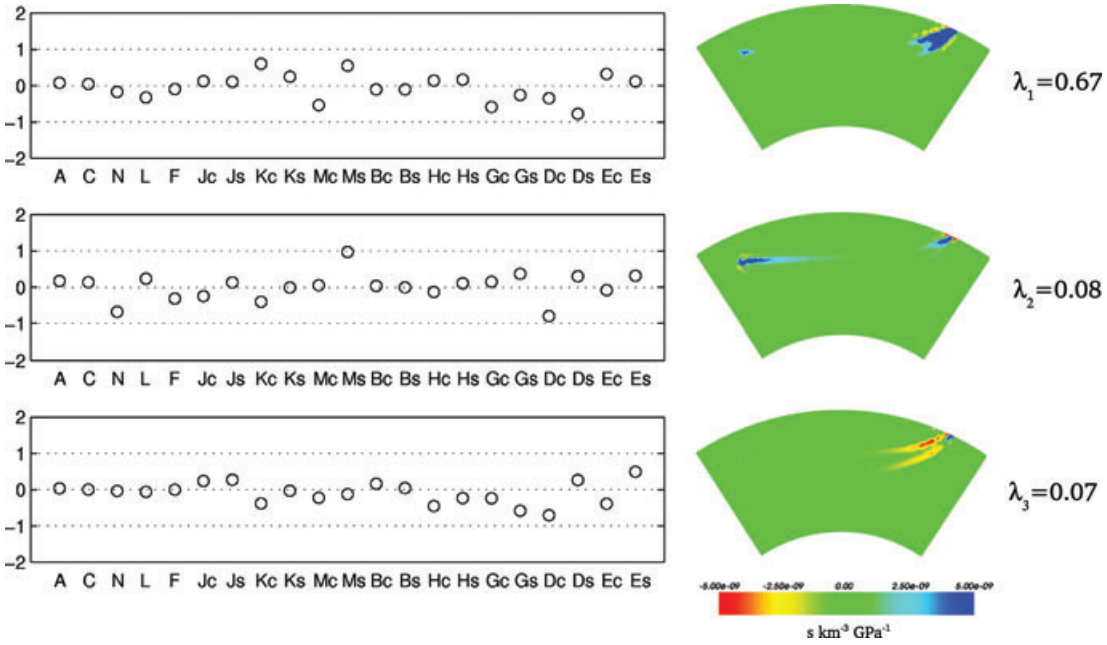

Figure 8. First three principal sensitivity kernels for the *S*-wave splitting intensity: (left-hand panels) coefficients u_{ki} of the linear combination linking the principal kernels K_{p_k} to the 21 asymptotic kernels K_{a_i} (eq. 9) and (right-hand panels) spatial patterns of the kernels plotted in the vertical source–receiver plane.

noted C. Station C is situated at an epicentral distance of 40° and corresponds to a source azimuthal angle of 220°, which makes station C receive slightly more Love-wave energy. For the Love wave at station B (Fig. 3), the average local azimuth along the path is about 130°, which leads to $K_N \simeq -K_{E_c}$ (Table 1). The kernels K_N and K_{E_c} therefore combine well with each other and $K_{p_1} \simeq K_N - K_{E_c}$ (Fig. 3). For the Love wave at station C, the average local azimuth along the path is about 240°. It is now K_{E_s} which combines well with $K_N (K_N \simeq -K_{E_s}$, Table 1). As a result, for this path K_{p_1} comes as $-K_N + K_{E_s}$ (Fig. 12). Although the sensitivity is not as well localized as for station B (Figs 2 and 9), the important asymptotic parameters are again N, $E_{c,s}$ and $M_{c,s}$, $D_{c,s}$ (Fig. 12). Love–Rayleigh coupling is also significant for this path, as revealed by the clear V-band pattern observed for K_{p_3} (Fig. 12).

These experiments with single source–receiver configurations demonstrate the efficiency of the principal component analysis to extract the essential elastic parameters for a given datum. Tomographic images are constructed based upon the sensitivity of

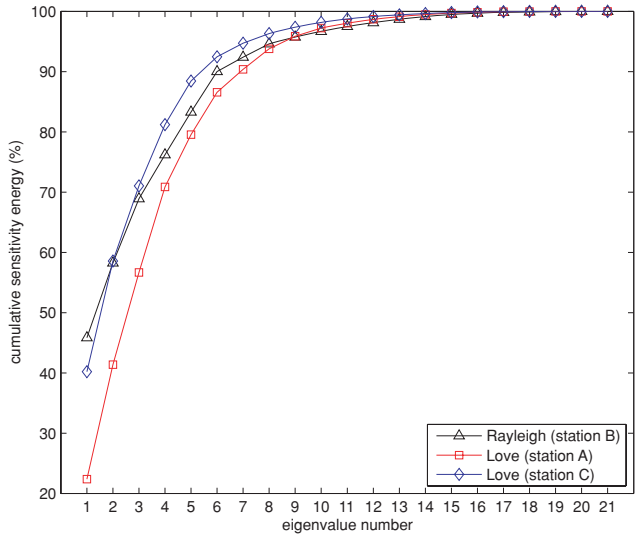

Figure 9. Cumulative sensitivity power for the 21 principal parameters p_k for the fundamental-mode Rayleigh wave at station B (triangles), the fundamental-mode Love wave at station A (squares) (i.e. when there is significant Love–Rayleigh coupling), and for the fundamental-mode Love wave at station C (diamonds).

an entire data set, that is, the combined sensitivity of numerous intersecting source–receiver paths. In the next section, we test the principal component analysis on a small synthetic data set.

4 APPLICATION TO INVERSE PROBLEMS

Tomographic inversions seek to minimize the misfit quantified by a certain relationship between observations ('data') and simulations ('synthetics'). For example, if we consider the traveltime difference $T^{\rm obs} - T^{\rm syn}$, the misfit function S may be defined as

$$S = \frac{1}{2} \sum_d \left(T_d^{\rm obs} - T_d^{\rm syn} \right)^2 , \tag{10}$$

where the summation is over all sources, receivers and picks. Minimization algorithms, for example, conjugate gradient methods, are often based upon derivatives of the misfit function with respect to the structural parameters we wish to image. These derivatives can be regarded as 'misfit kernels' (Tape *et al.* 2007), because they represent the sensitivity of the entire data set to a given model parameter. They are the sum of individual source–receiver kernels $K_d^{\rm sr}$ weighted by the measurements $T_d^{\rm obs} - T_d^{\rm syn}$

$$K^S = - \sum_d \left(T_d^{\rm obs} - T_d^{\rm syn} \right) K_d^{\rm sr} . \tag{11}$$

We test the principal component analysis on a synthetic misfit kernel for a simple source–receiver geometry. The experiment involves 62 stations (a subset of the Orfeus network; see http://www.orfeus-eu.org) and five events (one real event located in Crete and four fictitious earthquakes; Fig. 13). The reference signals are computed in isotropic PREM. We reduce the isotropic S-wave speed by 4 per cent everywhere in the crust to create the 'observed' signals. The observed signals are therefore associated with perturbations in the parameters N, L and F. We analyse the fundamental-mode Love wave between 40 and 100 s. Traveltime anomalies are measured by cross-correlating time-variable filtered transverse signals, as discussed previously. In previous sections we slightly smoothed the kernels by convolving them with a 3-D Gaussian with a half-width comparable to the shortest wavelength in the numerical simulations. For tomographic data in a certain period range, it seems more appropriate to consider a wavelength representative of the data set. The best-spatial resolution that can be achieved is likely to be higher than the shortest wavelength, depending on the source and receiver distribution. For this experiment, we apply smoothing to the basic

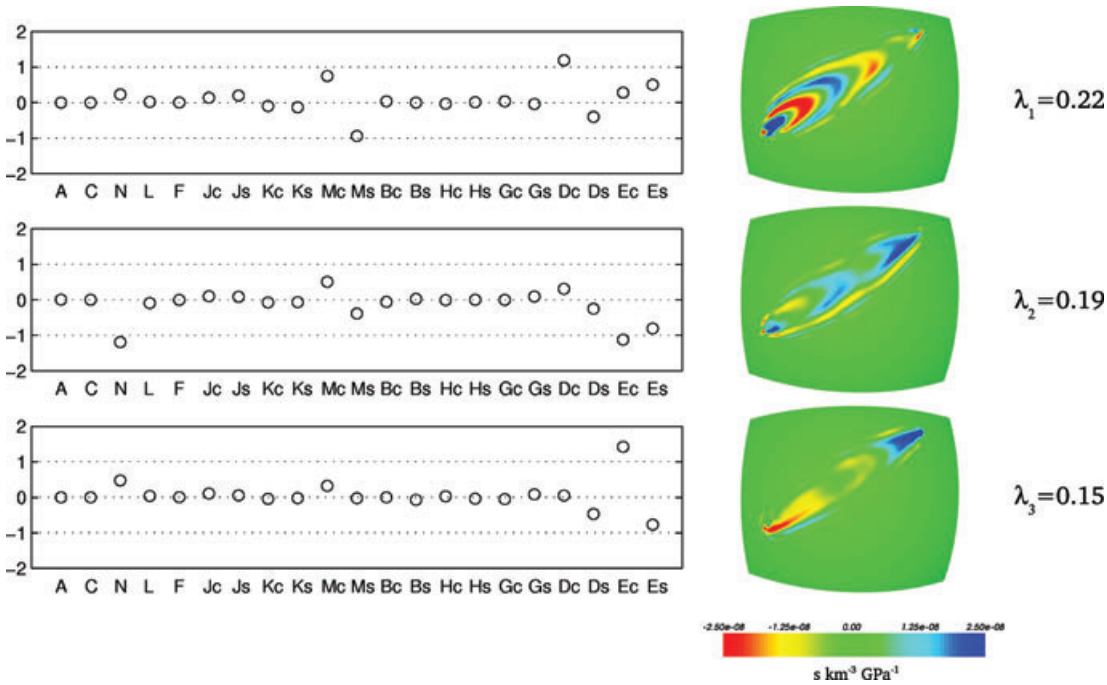

Figure 10. First three principal sensitivity kernels for the fundamental-mode Love wave in the presence of significant Rayleigh–Love coupling (station A): (left-hand panels) coefficients u_{ki} of the linear combination linking the principal kernels K_{p_k} to the 21 asymptotic kernels K_{a_i} (eq. 9) and (right-hand panels) spatial patterns of the kernels in map view at 75 km depth.

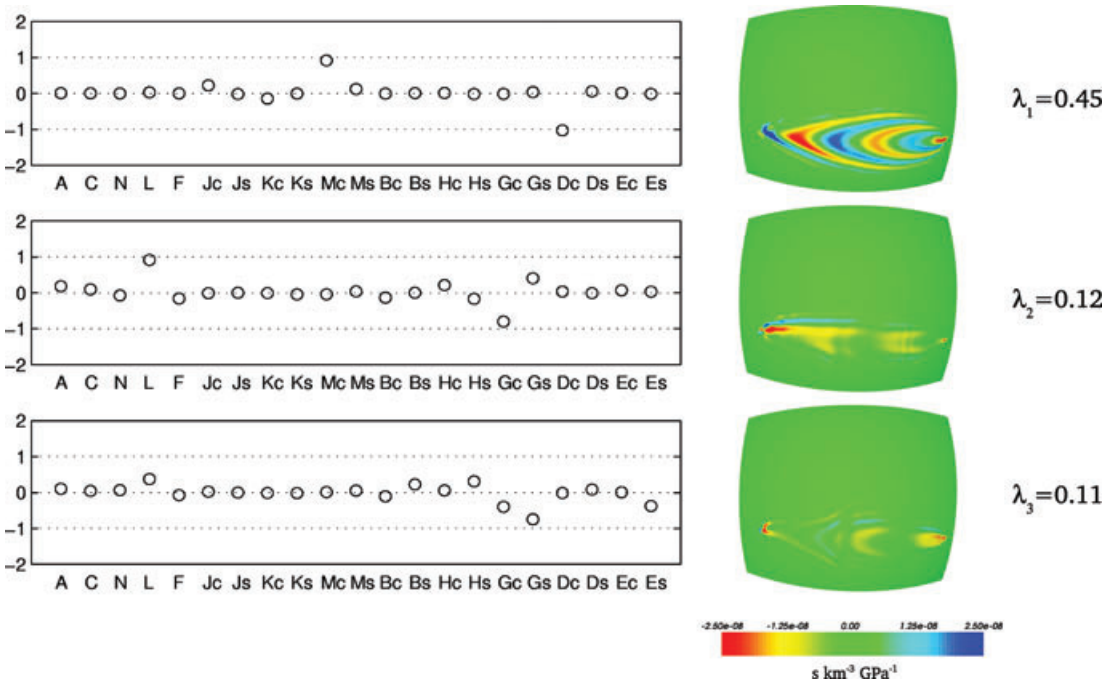

Figure 11. First three principal sensitivity kernels for the fundamental-mode Rayleigh wave when there is significant Love–Rayleigh coupling (station B): (left-hand panels) coefficients u_{ki} of the linear combination linking the principal kernels K_{p_k} to the 21 asymptotic kernels K_{a_i} (eq. 9) and (right-hand panels) spatial patterns of the kernels in map view at 75 km depth.

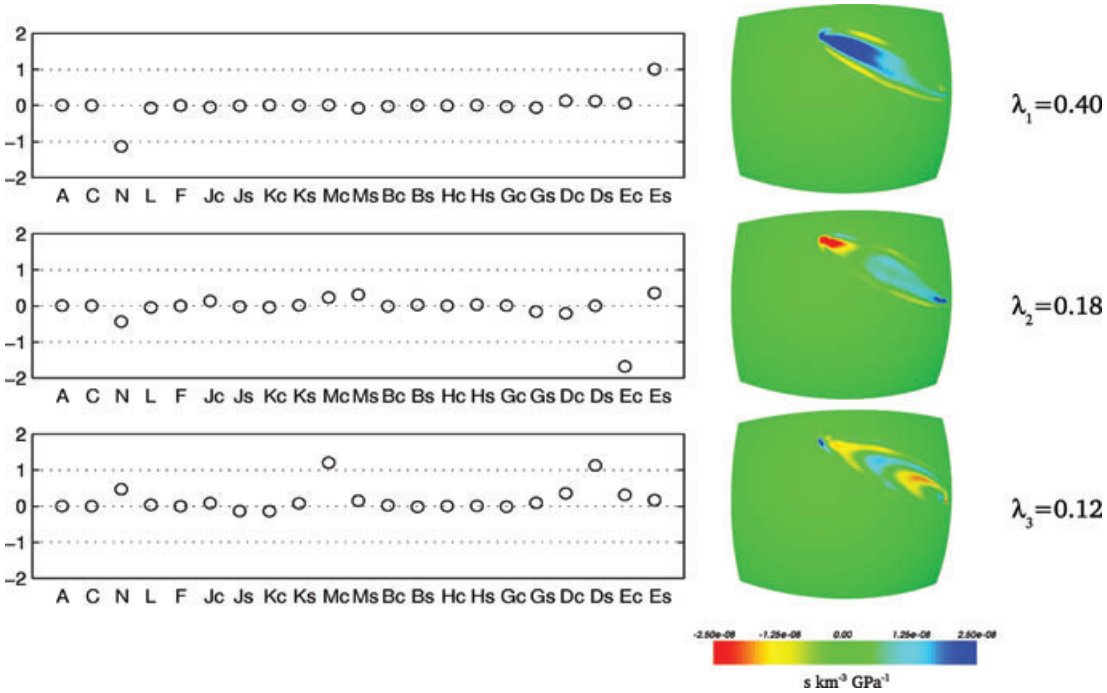

Figure 12. First three principal sensitivity kernels for the fundamental-mode Love wave on a path different from the one shown in Fig. 3 (station C): (left-hand panels) coefficients u_{ki} of the linear combination linking the principal kernels K_{p_k} to the 21 asymptotic kernels K_{a_i} (eq. 9) and (right-hand panels) spatial patterns of the kernels in map view at 75 km depth. The source is located on the right-hand side for this figure.

misfit kernels in agreement with Love-wave data in the period range 40 and 100 s. The half-width of the Gaussian function is set to half the minimum wavelength (85 km).

The principal component analysis again reveals that the sensitivity of this data set is accounted for by a small number of principal kernels. Four principal kernels describe nearly 90 per cent of the sensitivity power, and we reach more than 80 per cent with only three parameters (Fig. 14). It is interesting to note that in the context of a conjugate gradient method, the misfit kernels are scaled images of the model update that would be added to the laterally homogeneous reference model. We can therefore directly compare the principal misfit kernels to the 'real' model to estimate the

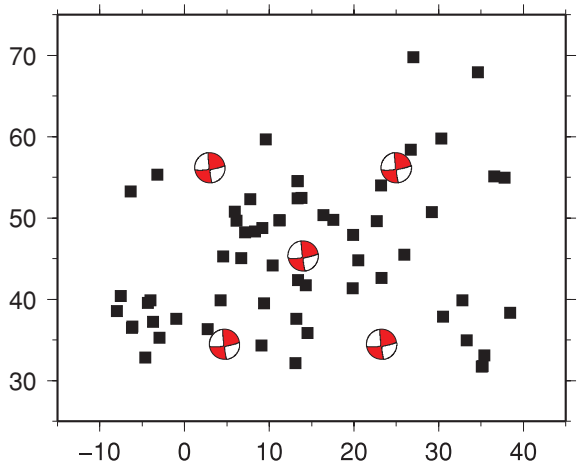

Figure 13. Location of the five events (beach balls) and the 62 stations (triangles) used in the computation of the fundamental-mode Love-wave misfit kernel. The stations correspond to a subset of the Orfeus network in the Euro-Mediterranean region. The event in the south-east is a real earthquake located in Crete at 12 km depth. The same source mechanism (from the Harvard centroid-moment tensor catalogue) is used for the other four simulations.

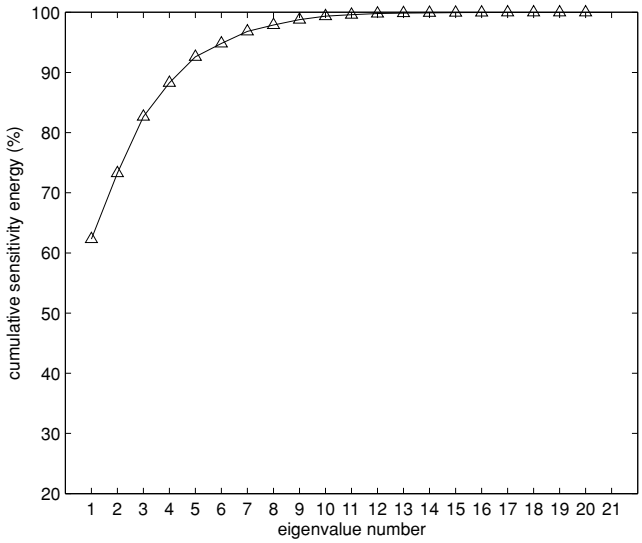

Figure 14. Cumulative sensitivity power for the 21 principal parameters p_k from the principal component analysis of the Love-wave misfit sensitivity for the source–receiver geometry shown in Fig. 13. We consider the fundamental-mode Love wave with periods between 40 and 100 s.

potential tomographic resolution. The first principal kernel is dominated by sensitivity to the parameter N (Fig. 15). This is the expected result for Love-wave data in a model with isotropic perturbations, Love waves being relatively insensitive to the parameters L and F (Section 4). The azimuthal anisotropic parameters ($E_{c,s}$, $D_{c,s}$ and $M_{c,s}$) contribute to the other principal kernels (Fig. 15). This represents the trade-off between spherically symmetric and azimuthal parameters. Note, however, that the kernels K_{p_2} and K_{p_3} in Fig. 15 have significant amplitude over small localized areas (in the vicinity of the sources and along the southern boundary of the region). This spatial pattern suggests that the imperfect resolution we obtain with this data set is mainly due to gaps in path coverage. Complete coverage of the targeted area with more uniform azimuthal sampling would further diminish the contributions of the azimuthal anisotropic parameters and lead to a better reconstruction of the 'real' model.

5 DISCUSSION

Sensitivity kernels for individual arrivals (Section 3) show that seismic waves are sensitive to just a few independent anisotropic model parameters. Most of the sensitivity is explained with a handful of principal sensitivity kernels. Our principal component analysis of the finite-frequency sensitivity proves to be a powerful tool for analysing and characterizing seismic waves. Although it is a purely mathematical and 'Earth-blind' analysis, without any regard for the kind of the data considered, it gives physically meaningful results. The analysis confirms the importance of the asymptotic parameters L and $G_{c,s}$ for fundamental-mode Rayleigh waves, N and $E_{c,s}$ for fundamental-mode Love waves, $J_{c,s}$ and $K_{c,s}$ for P waves and $G_{c,s}$ for *SKS*-splitting. It identifies the most significant parameters among all of those with a potential influence for S-wave splitting. It also highlights the role of $M_{c,s}$ and $D_{c,s}$ for surface waves, which dominate the sensitivity when significant Love–Rayleigh coupling is present. We expect this tool to be important for a better understanding of less-used and more complex portions of seismograms, such as multiple-reflected mantle P and S waves or surface wave overtones (Zhou 2009).

A major advantage of our analysis is that it can be directly incorporated in tomographic inversions. The principal component analysis will be applied to the 'misfit kernel' (the gradient of the misfit function) representing the sensitivity of the entire data set. Significant progress in imaging is likely to require a better exploitation of complete waveforms, which implies joint inversions of body and surface waves, as well as other portions of the seismograms. This is now possible thanks to recent progress in numerical methods and parallel computing, enabling tomography to consider full-wave propagation in 3-D media. Tomographic inversions using these advances in technology have already been tested (Chen *et al.* 2007; Tape *et al.* 2007). Automatic time-window selection algorithms required to build the necessarily huge data sets have also been developed (Maggi *et al.* 2009). We expect the associated misfit kernels to be quite complicated, due to the mixing of all the data sensitivities. It will be very difficult to identify 'by eye' the few relevant anisotropic parameters (c_i or a_i) in these kinds of inversions. The principal component analysis proposed here will be an essential tool to properly identify them.

If the sensitivity of a data set is described by a few principal kernels, the principal component analysis automatically identifies them. Based upon this information, we can invert the data set for the corresponding principal elastic parameters. The bias will be minimal, because these parameters are the ones to which the data set is most sensitive. Another major advantage of the principal component analysis is that it finds independent combinations of elastic parameters, whereas a simple selection of the primary (or asymptotic) kernels according to a threshold value may select parameters that the data set cannot constrain independently. The reduction of the number of parameters based upon the principal component analysis should therefore help to stabilize the inversion. Good azimuthal coverage of the targeted area is, however, required for sufficient resolution of the various parameters (Section 4). Once the selected principal parameters have been inverted for, the c_j or a_i can be updated by reversing the relationships given by eqs (8) and (A1). In an iterative inversion scheme (e.g. Tape *et al.* 2007), the selection of the elastic parameters should be performed at each iteration. The

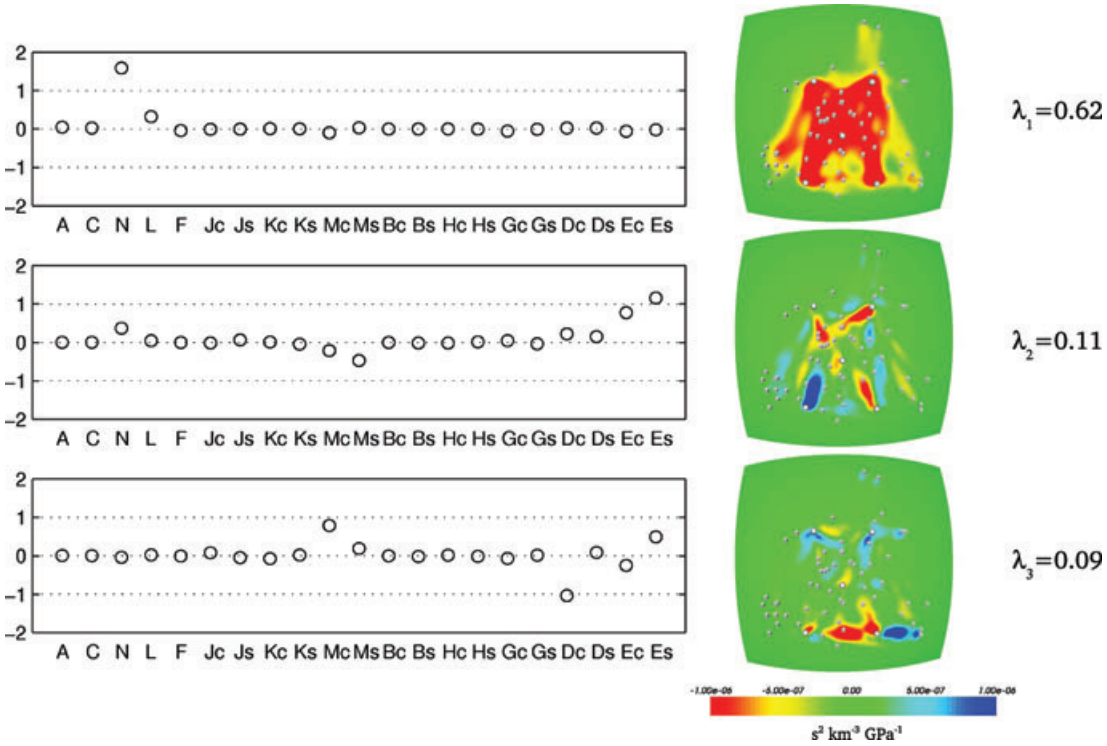

Figure 15. First three principal sensitivity kernels for the Love-wave misfit sensitivity for the source–receiver geometry shown in Fig. 13: (left-hand panels) coefficients u_{ki} of the linear combination linking the principal kernels K_{p_k} to the 21 asymptotic kernels K_{a_i} and (right-hand panels) spatial patterns of the kernels in map view at 75 km depth. The grey squares represent the receivers and the sources are located at the grey spheres.

final model obtained based upon this approach can be directly compared to mineral-physics predictions of the elastic tensor for mantle convection models (Becker *et al.* 2006). We can also use Browaeys & Chevrot's (2004) decomposition of the elastic tensor to extract the hexagonal component of the final model, from which a more traditional description of anisotropy in terms of a magnitude and direction can then be deduced.

The analysis can also take into account certain *a priori* knowledge regarding the distribution of anisotropy in the Earth. For example, if anisotropy is thought to be mainly present in the upper mantle, we may wish to select the parameters to which the sensitivity is maximal in this region only. This may be achieved by restricting the volume integrals in the definition of the **M** matrix (eq. 4) to the upper mantle.

As discussed previously, for tomography the principal component analysis will be applied once to the misfit kernel (the summed sensitivity of the data set for all events, all receivers, and all picks). When adjoint methods are combined with numerical modelling (as in SESAME), it is possible to calculate, based upon only one simulation, the sum of the kernels for all the data (all receivers and picks) corresponding to one event, that is, the 'event kernel' as defined by Tape *et al.* (2007). The misfit kernel is then the sum of these event kernels. The related computational time is mainly controlled by the number of events. This makes regional adjoint tomography feasible on moderate-size clusters (Tape *et al.* 2007; Chen *et al.* 2007). With our method, the calculation of the 21 primary sensitivity kernels has a computational cost that is basically the same as that associated with the calculation of isotropic sensitivity kernels, because it is the simulation of the forward and adjoint wavefields that determines the numerical cost, not the construction of the kernels. The most time-consuming part of the principal component analysis is the construction of the **M** matrix based upon the calculation of the volume integrals (eq. 4). Overall, the additional computational cost due to the principal component analysis is rather insignificant.

ACKNOWLEDGMENTS

We thank two reviewers for their comments and suggestions, which helped to improve the manuscript. The adjoint spectral-element computations discussed in this paper were performed on Caltech's Division of Geological & Planetary Sciences Dell cluster and at the Service Commun de Calcul Intensif de l'Observatoire de Grenoble (SCCI). The source code for the adjoint spectral-element simulations is freely available from www.geodynamics.org.

REFERENCES

Anderson, D.L., 1961. Elastic wave propagation in layered anisotropic media, *J. geophys. Res.,* **66,** 2953–2963.

Babuška, V. & Cara, M., 1991. *Seismic Anisotropy in the Earth*, Kluwer Academic, Dordrecht.

Backus, G.E., 1965. Possible forms of seismic anisotropy of the uppermost mantle under oceans, *J. geophys. Res.,* **70,** 3429–3439.

Becker, T.W., Chevrot, S., Schulte-Pelkum, V. & Blackman, D.K., 2006. Statistical properties of seismic anisotropy predicted by upper mantle geodynamic models, *J. geophys. Res.,* **111,** B08309, doi:10.1029/2005JB004095.

Browayes, J.T. & Chevrot, S., 2004. Decomposition of the elastic tensor and geophysical applications, *Geophys. J. Int.,* **159,** 667–678.

Chen, M. & Tromp, J., 2007. Theoretical and numerical investigation of global and regional seismic wave propagation in weakly anisotropic Earth models, *Geophys. J. Int.,* **168,** 1130–1152.

Chen, P., Zhao, L. & Jordan, T.H., 2007. Full 3D tomography for the crustal structure of the Los Angeles region, *Bull. seism. Soc. Am.,* **97,** 1094–1120.
Chevrot, S., 2000. Multichannel analysis of shear wave splitting, *J. geophys. Res.,* **105,** 21 579–21 590.
Chevrot, S., 2006. Finite-frequency vectorial tomography: a new method for high resolution imaging of mantle anisotropy, *Geophys. J. Int.,* **165,** 641–657.
Debayle, E., Kennett, B.L.N. & Priestley, K., 2005. Global azimuthal seismic anisotropy and the unique plate-motion deformation of Australia, *Nature,* **433,** 509–512.
Deschamps, F., Lebedev, S., Meier, T. & Trampert, J., 2008. Stratified seismic anisotropy reveals past and present deformation beneath the east-central United States *Earth planet. Sci. Lett.,* **274,** 489–498.
Dziewonski, A.M. & Anderson, D.L., 1981. Preliminary Reference Earth Model, *Phys. Earth planet. Inter.,* **25,** 297–356.
Favier, N. & Chevrot, S., 2003. Sensitivity kernels for shear wave splitting in transverse isotropic media, *Geophys. J. Int.,* **153,** 213–228.
Forsyth, D.W., 1975. The early structural evolution and anisotropy of the oceanic upper mantle, *Geophys. J. R. astr. Soc.,* **43,** 103–162.
Hess, H.H., 1964. Seismic anisotropy of the uppermost mantle under oceans, *Nature,* **203,** 629–631.
Kaminski, E. & Ribe, N.L.M., 2002. Timescales for the evolution of seismic anisotropy in mantle flow, *Geochem. Gephys. Geosyst.,* **3**(1), doi:10.1029/2001GC000222.
Komatitsch, D. & Tromp, J., 2002a. Spectral-element simulations of global seismic wave propagation—I. Validation, *Geophys. J. Int.,* **149,** 390–412.
Komatitsch, D. & Tromp, J., 2002b. Spectral-element simulations of global seismic wave propagation—II. Three-dimensional models, oceans, rotation and self-gravitation, *Geophys. J. Int.,* **150,** 303–318.
Landisman, M., Dziewonski, A. & Sato, Y., 1969. Recent improvements in the analysis of surface wave observations, *Geophys. J. R. astr. Soc.,* **17,** 369–403.
Lévêque, J.J., Debayle, E. & Maupin, V., 1998. Anisotropy in the Indian Ocean upper mantle from Rayleigh- and Love-waveform inversion, *Geophys. J. Int.,* **133,** 529–540.
Liu, Q. & Tromp, J., 2006. Finite-frequency kernels based upon adjoint methods, *Bull. seism. Soc. Am.,* **96,** 2383–2397.
Liu, Q. & Tromp, J., 2008. Finite-frequency sensitivity kernels for global seismic wave propagation based upon adjoint methods, *Geophys. J. Int.,* **174,** 265–286.
Long, M.D., de Hoop, M.V. & van der Hilst, R.D., 2007. Wave-equation shear wave splitting tomography, *Geophys. J. Int.,* **172,** 311–330.
Maggi, A., Tape, C., Chen, M., Chao, D. & Tromp, J., 2009. An automated time-window selection algorithm for seismic tomography, *Geophys. J. Int.,* **178,** 257–281.
Maupin, V. & Park, J., 2007. Theory and Observations - Wave propagation in anisotropic media, in *Treatise in Geophysics*,Vol. 1, pp. 289–321, eds Romanowicz, B. & Dziewonski, A.M., Elsevier, Amsterdam.
Marone, F. & Romanowicz, B., 2007. The depth distribution of azimuthal anisotropy in the continental upper mantle, *Nature,* **447,** 198–201.
Marquering, H., Dahlen, F.A. & Nolet, G., 1999. Three-dimensional sensitivity kernels for finite-frequency traveltimes: the banana-doughnut paradox, *Geophys. J. Int.,* **137,** 805–815.
Montagner, J.P., 1998. Where can seismic anisotropy be detected in the Earth's mantle? In boundary layers. . . , *Pure appl. geophys.,* **151,** 223–256.
Montagner, J.P. & Jobert, N., 1988. Vectorial tomography - II. Application to the Indian Ocean, *Geophys. J.,* **94,** 309–344.
Montagner, J.P. & Nataf, H.C., 1986. A simple method for inverting the azimuthal anisotropy of surface waves, *J. geophys. Res.,* **91,** 511–520.
Montagner, J.P. & Tanimoto, T., 1991. Global upper mantle tomography of seismic velocities and anisotropies, *J. geophys. Res.,* **96,** 20 337–20 351.
Montagner, J.P., Griot-Pommera, D.A. & Lavé, J., 2000. How to relate body wave and surface wave anisotropy? *J. geophys. Res.,* **105,** 19 015–19 027.
Panning, M.P. & Nolet, G., 2008. Surface wave tomography for azimuthal anisotropy in a strongly reduced parameter space, *Geophys. J. Int.,* **174,** 629–648.
Silver, P.G., 1996. Seismic anisotropy beneath the continents: probing the depths of geology, *Annu. Rev. Earth planet. Sci.,* **24,** 385–432.
Sieminski, A., Liu, Q., Trampert, J. & Tromp, J., 2007a. Finite-frequency sensitivity of surface waves to anisotropy based upon adjoint methods, *Geophys. J. Int.,* **168,** 1153–1174.
Sieminski, A., Liu, Q., Trampert, J. & Tromp, J., 2007b. Finite-frequency sensitivity of body waves to anisotropy based upon adjoint methods, *Geophys. J. Int.,* **171,** 368–389.
Sieminski, A., Paulssen, H., Trampert, J. & Tromp, J., 2008. Finite-frequency SKS splitting: measurement and sensitivity kernels, *Bull. seism. Soc. Am.,* **98,** 1797–1810.
Simons, F.J., van der Hilst, R.D., Montagner, J.P. & Zielhuis, A., 2002. Multimode Rayleigh wave inversion for shear wave speed heterogeneity and azimuthal anisotropy of the Australian upper mantle, *Geophys. J. Int.,* **151,** 738–754.
Smith, M.L. & Dahlen, F.A., 1973. The azimuthal dependence of Love and Rayleigh wave propagation in a slightly anisotropic medium, *J. geophys. Res.,* **78,** 3321–3333.
Tape, C., Liu, Q. & Tromp, J., 2007. Finite frequency tomography using adjoint methods—methodology and examples using membrane surface waves, *Geophys. J. Int.,* **168,** 1105–1129.
Tarantola, A., 1984. Inversion of seismic reflection data in acoustic approximation, *Geophysics,* **49,** 1259–1266.
Thomsen, L., 1986. Weak anisotropy, *Geophysics,* **51,** 1954–1966.
Trampert, J. & van Heijst, H.J., 2002. Global azimuthal anisotropy in the transition zone, *Science,* **296,** 1297–1299.
Tromp, J., Tape, C. & Liu, Q., 2005. Seismic tomography, adjoint methods, time reversal and banana-doughnut kernels, *Geophys. J. Int.,* **160,** 195–216.
Vinnik, L.P., Farra, V. & Romanowicz, B., 1989. Azimuthal anisotropy in the Earth from observations of SKS at Geoscope and NARS broadband stations, *Bull. seism. Soc. Am.,* **79,** 1542–1558.
Zhang, S. & Karato, S.-I., 1995. Lattice preferred orientation of olivien aggregates deformed in simple shear, *Nature,* **375,** 774–777.
Zhao, L. & Jordan, T.H., 2006. Structural sensitivities of finite-frequency seismic waves: a full-wave approach, *Geophys. J. Int.,* **165,** 981–990.
Zhao, L., Jordan, T.H., Olsen, K.B. & Chen, P., 2005. Fréchet kernels for imaging regional Earth structure based on three-dimensional reference models, *Bull. seism. Soc. Am.,* **95,** 2066–2080.
Zhou, Y., 2009. Multimode surface wave sensitivity kernels in radially anisotropic earth media, *Geophys. J. Int.,* **176,** 865–888.
Zhou, Y., Dahlen, F.A. & Nolet, G., 2004. Three-dimensional sensitivity kernels for surface wave observables, *Geophys. J. Int.,* **158,** 142–168.

APPENDIX A: ALTERNATIVE DESCRIPTIONS OF ANISOTROPY

The 21 elastic parameters C_{IJ}, $I, J = 1, \ldots, 6$, using Voigt's notation with contracted indices, are related to the elements of the elastic tensor c_{klmn}, $k, l, m, n = 1, 2, 3$, in spherical coordinates ($\hat{\mathbf{r}}$ pointing upward, $\hat{\boldsymbol{\theta}}$ to the south and $\hat{\boldsymbol{\phi}}$ to the east) such that

$$\begin{pmatrix} C_{11} & C_{12} & C_{13} & C_{14} & C_{15} & C_{16} \\ & C_{22} & C_{23} & C_{24} & C_{25} & C_{26} \\ & & C_{33} & C_{34} & C_{35} & C_{36} \\ & & & C_{44} & C_{45} & C_{46} \\ & & & & C_{55} & C_{56} \\ & & & & & C_{66} \end{pmatrix} = \begin{pmatrix} c_{\theta\theta\theta\theta} & c_{\theta\theta\phi\phi} & c_{\theta\theta rr} & c_{\theta\theta\phi r} & c_{\theta\theta\theta r} & c_{\theta\theta\theta\phi} \\ & c_{\phi\phi\phi\phi} & c_{\phi\phi rr} & c_{\phi\phi\phi r} & c_{\phi\phi\theta r} & c_{\phi\phi\theta\phi} \\ & & c_{rrrr} & c_{rr\phi r} & c_{rr\theta r} & c_{rr\theta\phi} \\ & & & c_{\phi r\phi r} & c_{\phi r\theta r} & c_{\phi r\theta\phi} \\ & & & & c_{\theta r\theta r} & c_{\theta r\theta\phi} \\ & & & & & c_{\theta\phi\theta\phi} \end{pmatrix}. \quad \text{(A1)}$$

The 21 anisotropic elastic parameters of Chen & Tromp (2007) are given in terms of these parameters by the following relations:

$$
\begin{aligned}
A &= \tfrac{1}{8}(3C_{11} + 3C_{22} + 2C_{12} + 4C_{66}),\\
C &= C_{33},\\
N &= \tfrac{1}{8}(C_{11} + C_{22} - 2C_{12} + 4C_{66}),\\
L &= \tfrac{1}{2}(C_{44} + C_{55}),\\
F &= \tfrac{1}{2}(C_{13} + C_{23}),\\
J_c &= \tfrac{1}{8}(3C_{15} + C_{25} + 2C_{46}),\\
J_s &= \tfrac{1}{8}(C_{14} + 3C_{24} + 2C_{56}),\\
K_c &= \tfrac{1}{8}(3C_{15} + C_{25} + 2C_{46} - 4C_{35}),\\
K_s &= \tfrac{1}{8}(C_{14} + 3C_{24} + 2C_{56} - 4C_{34}),\\
M_c &= \tfrac{1}{4}(C_{15} - C_{25} + 2C_{46}),\\
M_s &= \tfrac{1}{4}(C_{14} - C_{24} - 2C_{56}),\\
G_c &= \tfrac{1}{2}(C_{55} - C_{44}),\\
G_s &= -C_{45},\\
B_c &= \tfrac{1}{2}(C_{11} - C_{22}),\\
B_s &= -(C_{16} + C_{26}),\\
H_c &= \tfrac{1}{2}(C_{13} - C_{23}),\\
H_s &= -C_{36},\\
D_c &= \tfrac{1}{4}(C_{15} - C_{25} - 2C_{46}),\\
D_s &= \tfrac{1}{4}(C_{14} - C_{24} + 2C_{56}),\\
E_c &= \tfrac{1}{8}(C_{11} + C_{22} - 2C_{12} - 4C_{66}),\\
E_s &= -\tfrac{1}{2}(C_{16} - C_{26}).
\end{aligned}
\tag{A2}
$$